

Modeling bubbles and dissolved gases in the ocean

Jun-Hong Liang,¹ James C. McWilliams,¹ Peter P. Sullivan,² and Burkard Baschek¹

Received 5 August 2010; revised 3 December 2010; accepted 30 December 2010; published 8 March 2011.

[1] We report on the development of a bubble concentration model and a dissolved gas concentration model for the oceanic boundary layer. The bubble model solves a set of concentration equations for multiple gases in bubbles of different sizes, and the dissolved gas concentration model simulates the evolution of dissolved gases and dissolved inorganic carbon. The models include the effects of advection, diffusion, bubble buoyant rising, bubble size changes, gas exchange between bubbles and ambient water, and chemical reactions associated with the dissolution of CO₂. The formulation consistency and the numerical accuracy are shown by the good agreement with a model describing individual bubble behavior in a test simulating the evolution of a bubble cloud released in the water. To study the bubble and dissolved gas evolution after a single wave-breaking event, the models are coupled with a fluid dynamical Direct Numerical Simulation model with spatially and temporally distributed momentum and bubble injection for a typical breaking wave. The modeled bubble size spectrum compares well with laboratory measurements. The breaker-induced vortex not only advects the bubble-induced dissolved gas anomalies downstream but also entrains the surface diffusion layer to greater depth. Due to the hydrostatic pressure and surface tension exerted on bubbles, gases inside bubbles are able to dissolve in slightly supersaturated water. When the water is highly supersaturated, bubbles add to the venting of dissolved gases.

Citation: Liang, J.-H., J. C. McWilliams, P. P. Sullivan, and B. Baschek (2011), Modeling bubbles and dissolved gases in the ocean, *J. Geophys. Res.*, 116, C03015, doi:10.1029/2010JC006579.

1. Introduction

[2] Gas bubbles are ubiquitous in the ocean mixed layer and are commonly observed both at the ocean surface [e.g., Monahan, 2001; Melville and Matusov, 2002] and in ocean boundary layer [e.g., Zedel and Farmer, 1991; Thorpe *et al.*, 2003]. After their injection at the ocean surface due to the breaking of ocean surface waves, they are mixed and redistributed by the turbulent ocean boundary layer flows and rise toward the sea surface due to their own buoyancy. They are compressed when they are subducted, and expand when they rise. They also change size due to the gas exchange between bubbles and ambient water. They are lost by either bursting at the sea surface or fully dissolving into the ocean. The dissolved gases in the ocean are mixed and redistributed by the turbulent flows in the ocean boundary layer, and diffuse in and out of the water through the ocean surface as well as bubbles.

[3] Gas bubbles are important in the upper ocean as they change the acoustical and optical properties of water [e.g., Lamarre and Melville, 1994; Zhang *et al.*, 1998; Terrill *et al.*,

2001]. Due to their unique acoustical and optical properties, they are used as flow tracers to identify upper ocean processes like Langmuir circulations [e.g., Thorpe, 1982; Farmer and Li, 1995] and tidal fronts [Baschek *et al.*, 2006]. Bubbles provide an important pathway for air-sea gas exchange [e.g., Keeling, 1993; McNeil and D'Asaro, 2007; Stanley *et al.*, 2009]. Compressed by hydrostatic pressure and surface tension in addition to atmospheric pressure, gases inside bubbles can dissolve into the water even when the water is slightly supersaturated [e.g., Woolf and Thorpe, 1991; Woolf, 1997; D'Asaro and McNeil, 2007; Woolf *et al.*, 2007]. Bubbles also influence the upper ocean dynamics. They enhance stratification in the near-surface layer where they are abundant and weaken the downwelling branches of Langmuir cells [Smith, 1998].

[4] Compared to the extensive modeling studies on upper ocean dynamical processes like shear turbulence, convective turbulence, and Langmuir turbulence [e.g., Coleman *et al.*, 1990; Li *et al.*, 2005; Sullivan and McWilliams, 2010], bubble modeling in the upper ocean is relatively rare [Memery and Merlivat, 1985; Woolf and Thorpe, 1991; Vagle *et al.*, 2001; Thorpe *et al.*, 2003]. These models either trace individual bubbles [e.g., Woolf and Thorpe, 1991] or simulate only one size class of bubbles [Thorpe *et al.*, 2003]. They cannot be coupled with turbulence-resolving models and dissolved gas models. All these aspects preclude a realistic study of bubble behavior and bubble effects in the upper ocean.

¹Department of Atmospheric and Oceanic Sciences, University of California, Los Angeles, California, USA.

²Mesoscale and Microscale Meteorology Division, National Center for Atmospheric Research, Boulder, Colorado, USA.

[5] We aim to develop a multisize, multigas component bubble concentration model and a dissolved gas model that are suitable to be coupled with turbulence-resolving dynamic models for the oceanic boundary layers [McWilliams *et al.*, 1997; Sullivan *et al.*, 2004, 2007; Sullivan and McWilliams, 2010]. Our models incorporate essential bubble behavior and the impact of bubbles on dissolved gases, and are suitable for the study of bubble evolution and gas exchange. Section 2 describes the bubble model and the dissolved gas model. Section 3 demonstrates the accuracy of model formulation and implementation. Section 4 presents modeling results of bubbles and dissolved gases due to a single breaking wave. Section 5 is a summary.

2. Model Description

[6] The main modeling components are an upper ocean dynamic model, a size-resolving bubble model, and a dissolved gas model. They are described in sections 2.1, 2.2, and 2.3, respectively.

2.1. Upper Ocean Dynamic Model

[7] The dynamic model describes the water flows in an ocean boundary layer and provides the velocity field (\vec{u}) that advects and diffuses bubbles and dissolved gases. The velocity field can be a simple flow like a steady downwelling current, or the solutions from a model that resolved turbulence like a Direct Numerical Simulation (DNS) model [e.g., Sullivan *et al.*, 2004] or a Large Eddy Simulation (LES) model [e.g., McWilliams *et al.*, 1997; Sullivan *et al.*, 2007; Sullivan and McWilliams, 2010] for the oceanic boundary layer. In the current study, both a steady downwelling current and a DNS model are used. The DNS model together with a breaker model have been shown to accurately reproduce flow fields generated by a single wave-breaking event [Sullivan *et al.*, 2004].

[8] Gas bubbles in the upper ocean are not truly passive, as they are believed to play a role in upper ocean dynamics due to their buoyancy. The dynamic effect of bubbles, however, is not considered in the current study. We should mention that there is no formulation difficulty in including the dynamic effect and coupling the bubble model and the dissolved gas model with a LES model that is capable of simulating shear, convective, and Langmuir turbulence [Sullivan and McWilliams, 2010]. These will be presented in a future paper.

2.2. Bubble Model

[9] The concentration of gas m ($m = 1$ for O_2 , $m = 2$ for N_2 , and $m = 3$ for CO_2) in bubbles of radius $[r - \frac{\delta r}{2}, r + \frac{\delta r}{2}]$ at the unit volume centered at location \vec{x} , and time t is denoted as $n_m^{tot}(\vec{x}, r, t)$. Inside each individual bubble of this radius, the gas amount is $n_m(\vec{x}, r, t) = \frac{n_m^{tot}(\vec{x}, r, t)}{C_b(\vec{x}, r, t)}$ with $C_b(\vec{x}, r, t)$ the number concentration of bubbles of radius $[r - \frac{\delta r}{2}, r + \frac{\delta r}{2}]$ at the unit volume centered at \vec{x} and time t . The evolution of $n_m^{tot}(\vec{x}, r, t)$ is described as

$$\frac{\partial n_m^{tot}}{\partial t} = -\vec{u} \cdot \nabla n_m^{tot} - \nabla \cdot \vec{F}_m - \frac{\partial w^b n_m^{tot}}{\partial z} - \frac{\partial}{\partial r} \left(\frac{dr}{dt} n_m^{tot} \right) + \frac{dn_m}{dt} C_b + \frac{Q}{4P\pi r^3 / (3RT)} \chi_m^{atm}. \quad (1)$$

The first and the second terms on the right hand side represent advection and diffusion, where \vec{u} is the velocity vector and \vec{F}_m is the diffusion flux. The third term on the right hand side represents vertical advection due to bubble buoyancy. w^b is the rise velocity due to buoyancy and is calculated with the formulas suggested by Woolf and Thorpe [1991]. The fourth term on the right hand side represents bubble size changes. When a bubble changes size, it may go from one size bin ($[r - \frac{\delta r}{2}, r + \frac{\delta r}{2}]$) to another one. The fifth term on the right hand side is the gain/loss of gases due to gas exchange between bubbles and the ambient water. dn_m/dt is the rate of change of the gas amount inside a bubble. The last term on the right hand side is the injection of gases due to breaking waves. $Q(\vec{x}, r, t)$ is the bubble volume creation rate by breaking waves. The determination of dr/dt , dn_m/dt , and Q will be discussed later. $\chi_m(\vec{x}, r, t) = \frac{n_m^{tot}(\vec{x}, r, t)}{\sum_m n_m^{tot}(\vec{x}, r, t)}$ is the mole fraction of gas m inside the injected bubbles. P is the total pressure of the gas in the bubbles. T is the temperature of the gas, and R is the universal gas constant.

[10] The total pressure P exerted on the gases in a bubble is given by

$$P = p + p_{atm} + \frac{2\gamma}{r}, \quad (2)$$

where p is the hydrostatic pressure of the water column so that $\frac{dp}{dz} = -\rho g(w + w^b)$; p_{atm} is the atmospheric pressure; γ is the surface tension coefficient. At the ocean surface without bubbles, $P = p_{atm}$. The combination of the ideal gas law and Dalton's law yields

$$P \frac{4}{3} \pi r^3 = \sum_m n_m RT. \quad (3)$$

[11] The change of the amount of gas in a bubble can be related to the pressure difference between the partial pressure in the bubble and the partial pressure in the ambient water as [Thorpe, 1982]

$$\frac{dn_m}{dt} = -4\pi r D_m Nu_m \left[S_m \chi_m \left(p + p_{atm} + \frac{2\gamma}{r} \right) - c_m^* \right], \quad (4)$$

where $c_m^*(\vec{x}, t)$ is the dissolved gas concentration in the water; Nu is the Nusselt number defined as the ratio between the total gas flux and the molecular diffusive flux across the bubble surface; S is the Bunsen solubility; D is the diffusivity. Nu , S , and D are all calculated with formulas from Woolf and Thorpe [1991]. According to those formulas, the gas transfer rate for clean bubbles is slightly larger than for dirty bubbles. It also increases with bubble speed and background turbulence, and decreases with bubble radius. Saturation level σ_m is calculated as $\sigma_m = \frac{c_m^*}{S_m \chi_m^{atm} p_{atm}} \times 100\%$ with χ_m^{atm} the percentage of gas m in the atmosphere. In the absence of bubbles, dissolved gases are in equilibrium with the atmosphere when the water is 100% saturated. In the presence of bubbles, there is still a gas flux from the bubbles to the water when $\sigma = 100\%$ due to the addition of hydrostatic pressure and surface tension (equation (4)). The equilibrium saturation level is higher than 100%. The effect of bubbles on dissolved gases is larger when bubbles are brought to a greater depth and when surface tension is larger.

[12] The rate of change of the bubble radius can be obtained by combining equations (2)–(4)

$$\frac{dr}{dt} = \left[\frac{3RT}{4\pi r^2} \sum_m \frac{dn_m}{dt} - r \frac{dp}{dt} \right] \left(3p + 3p_{atm} + \frac{4\gamma}{r} \right)^{-1}. \quad (5)$$

The bubble number concentration C_b is calculated at each time step diagnostically as

$$C_b = \frac{3RT}{4P\pi r^3} \sum_m n_m^{tot}. \quad (6)$$

[13] Our bubble model has the same spirit as *Thorpe et al.* [2003], who solve an equation for the number concentration C_b of bubbles of a particular size. In both models, gas dissolution and buoyant rising are considered, while bubble distortion and bubble fragmentation/coalescence are neglected, as they have been shown to have a negligible effect on bubble evolution [*Thorpe et al.*, 2003]. The major generalizations of the current model over the model by *Thorpe et al.* [2003] are (1) bubbles of different sizes are included, (2) the fractions of different gases evolve with time, (3) the effect of ambient pressure change on bubble size change is included, and (4) the bubble model can be easily coupled with a dissolved gas model and an upper ocean dynamic model where ocean boundary layer turbulence is resolved instead of parameterized. These generalizations allow for a better understanding of bubble evolution and the effects of bubbles on upper ocean dynamics and gas exchange.

[14] Besides the concentration approach adopted in this study, we can also model bubble evolution using a single-bubble model, which tracks individual bubbles in a background flow [*Memery and Merlivat*, 1985; *Woolf and Thorpe*, 1991; *Vagle et al.*, 2001; *Baschek et al.*, 2006]. At each time, the location of an individual bubble \vec{x} , is calculated as

$$\frac{d\vec{x}}{dt} = \vec{u} + w^b \mathbf{z}, \quad (7)$$

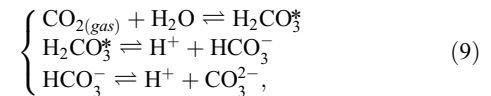
with \mathbf{z} the unit vector of the vertical direction. The bubble radius (r), and the amount of gas m (n_m) in the bubble are calculated using equations (4) and (5). Equations (4), (5), and (7) are solved for each individual bubble. The concentration model includes the same bubble physics as this single bubble model when the velocity field is the same. Compared to the concentration model, the single bubble model is algorithmically easier to implement. It circumvents the numerical dispersion and dissipation errors that arise when solving advection-diffusion equations. However, the single bubble model also has limitations. It is not easy to couple a single bubble model with a dissolved gas model and a dynamic model, and it is impossible to follow a very large number of bubbles in the ocean. The use of an individual bubble for ocean flows invokes the assumption that the gross behavior of the numerous bubbles can be inferred from a few representative samples. While this assumption is adequate for simple background flows, it is not feasible to follow enough individual bubbles to sustain a good spatial sampling density in a chaotic surface boundary layer.

2.3. Dissolved Gas Model

[15] We first define c_m as

$$c_m = \begin{cases} c_m^* & \text{when } m \neq 3 \\ [\text{DIC}] = [\text{CO}_3^{2-}] + [\text{HCO}_3^-] + c_3^* & \text{when } m = 3, \end{cases} \quad (8)$$

with the square brackets denoting the concentration of the chemical species and c_m^* the concentration of dissolved gas m . c_m denotes dissolved gases except for CO_2 . The dissolution of CO_2 simultaneously leads to the following three chemical reactions [*Sarmiento and Gruber*, 2006]



where H_2CO_3^* is the dissolved CO_2 with carbonic acid, HCO_3^- is bicarbonate, and CO_3^{2-} is carbonate. The partition in the global surface water among the above three species is 0.5%, 88.6%, and 10.9%. These values are determined by temperature, salinity, and alkalinity, which is a measure of the excess of bases over acids [*Sarmiento and Gruber*, 2006]. The ocean would take up much less atmospheric CO_2 if there were no chemical reactions to convert dissolved CO_2 into HCO_3^- and CO_3^{2-} . In the model, c_m^* is diagnosed from c_m using the iterative procedure described by *Sarmiento and Gruber* [2006], and an alkalinity of 2.2 equivalent per liter is assumed.

[16] The governing equation for c_m is a set of advection-diffusion equations with source/sink terms relating the gas exchange between the atmosphere through the ocean surface and bubbles. It can be written as

$$\frac{\partial c_m}{\partial t} = -\vec{u} \cdot \nabla c_m - \nabla \cdot \vec{F}_m + \int \frac{dn_m}{dt} C_b dr. \quad (10)$$

The first two terms on the right hand side of the above equation are advection and diffusion, with \vec{F}_m the diffusion flux. At the ocean surface ($z=0$), \vec{F}_m is calculated as $\vec{F}_m \cdot \mathbf{z} = k(S_m \chi_{atm} P_{atm} - c_m^*)$ with k the piston velocity [*Wanninkhof et al.*, 2009]. The representation of the piston velocity k will be discussed later when it is used in this study. The bubble concentration model and the dissolved gas model are coupled through the gas exchange between bubbles and the ambient water. This effect is represented by the last term of equation (10) and the fourth and fifth term at the right hand side of equation (1) together with equation (4).

2.4. Computational Implementation

[17] All the model components described above use the spatial differencing and time advancement schemes described by *Sullivan et al.* [1996], i.e., pseudospectral differencing in (x, y) planes, second-order finite differences in the z and r directions, and a third-order explicit Runge-Kutta method in time advancement. The single bubble model is also advanced using a third-order explicit Runge-Kutta scheme.

3. A Bubble Cloud in a Downwelling Current

[18] In this section, the ability of the model is tested by simulating the evolution of a bubble cloud of an idealized initial size distribution released at specified depths. In the test,

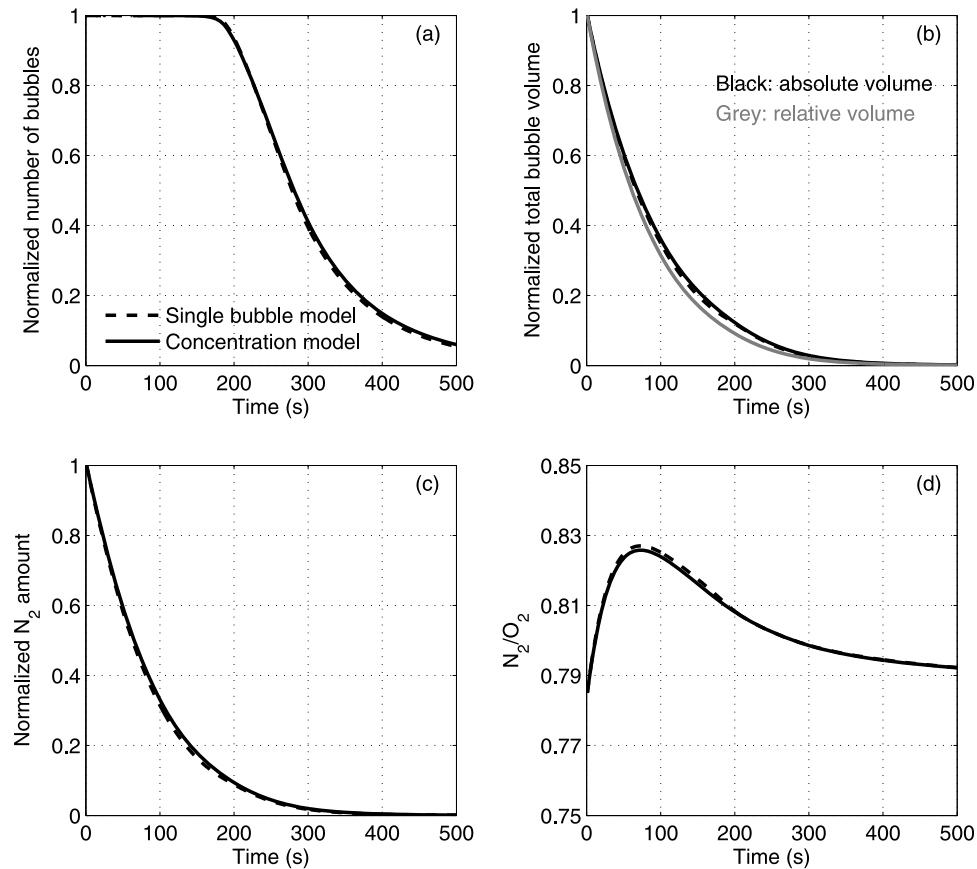


Figure 1. The evolution of (a) normalized total bubble number, (b) normalized total bubble volume, (c) normalized total N₂ amount, and (d) ratio between N₂ and O₂. (Dashed line is the solutions from the single bubble model; solid line is the solutions from the concentration model.)

an equal amount of bubbles of radius between 150 μm and 200 μm are released between 5 m and 10 m in the ocean that has a 0.005 m/s downwelling current. There is no current in either horizontal direction. The constant background downwelling current permits the use of an individual bubble model. The relative small bubble size, the deep release location, and the constant downwelling current all favor the persistence of bubbles in the water while the discontinuity in the initial bubble distribution adds a challenge to the modeling. Only N₂ and O₂ are considered in this test; CO₂ will be included in the next test. The dissolved gases are considered to be constant at 100% saturation during the time advancement because the dissolved gas amount is not being estimated in the single bubble model. In the single bubble model, 50,000 bubbles equally spaced at depth of [5 10]m and radius of [150 200] μm are released. In the concentration model, there are 48 stretched vertical levels covering the upper 20 m and 200 uniform bubble size bins covering 0 to 800 μm .

[19] With a 0.005 m/s downwelling current, bubbles of radius smaller than 50 μm have a buoyant rising speed smaller than the downwelling speed, and thus will be subducted. Bubbles with a radius larger than 50 μm will rise. All bubbles will rise right after their release, as they are all larger than 50 μm . At the same time, the partial pressure of gases inside the bubbles is much higher than their dissolved gases pressure due to the hydrostatic pressure and surface tension

exerted on the bubbles. This leads to the dissolution of gases into the water although the water is 100% saturated.

[20] Figure 1 shows the evolution of the normalized bubble number $\left(\frac{\int C_b(t)drdV}{\int C_b(0)drdV}\right)$, the normalized absolute bubble volume $\left(\frac{\int (n_1^{tot}(t)+n_2^{tot}(t))RT/PdrdV}{\int (n_1^{tot}(0)+n_2^{tot}(0))RT/PdrdV}\right)$, the normalized relative bubble volume $\left(\frac{\int (n_1^{tot}(t)+n_2^{tot}(t))RT/P_{am}drdV}{\int (n_1^{tot}(0)+n_2^{tot}(0))RT/P_{am}drdV}\right)$, the normalized N₂ amount inside bubbles $\left(\frac{\int n_2^{tot}(t)dV}{\int n_2^{tot}(0)dV}\right)$, and the N₂ to O₂ ratio inside bubbles $\left(\frac{\int n_2^{tot}(t)dV}{\int n_1^{tot}(t)dV}\right)$ in Figures 1a–1d. The results from the single bubble model are also plotted in Figure 1. Both models agree well with each other. The total number of bubbles stays constant for the first 180 s (Figure 1a). During this period, bubbles rise rapidly to the surface while the gases inside the bubbles dissolve into the water. No gas bubbles reach the surface or fully dissolve into the water because bubbles are injected at depths larger than 5 m. Although the total number of bubbles does not change, the total bubble volume decreases significantly (Figure 1b). The relative bubble volume decreases faster than the absolute bubble volume because the hydrostatic pressure exerted on bubble decrease when bubbles rise. Both gases dissolve rapidly into the ambient

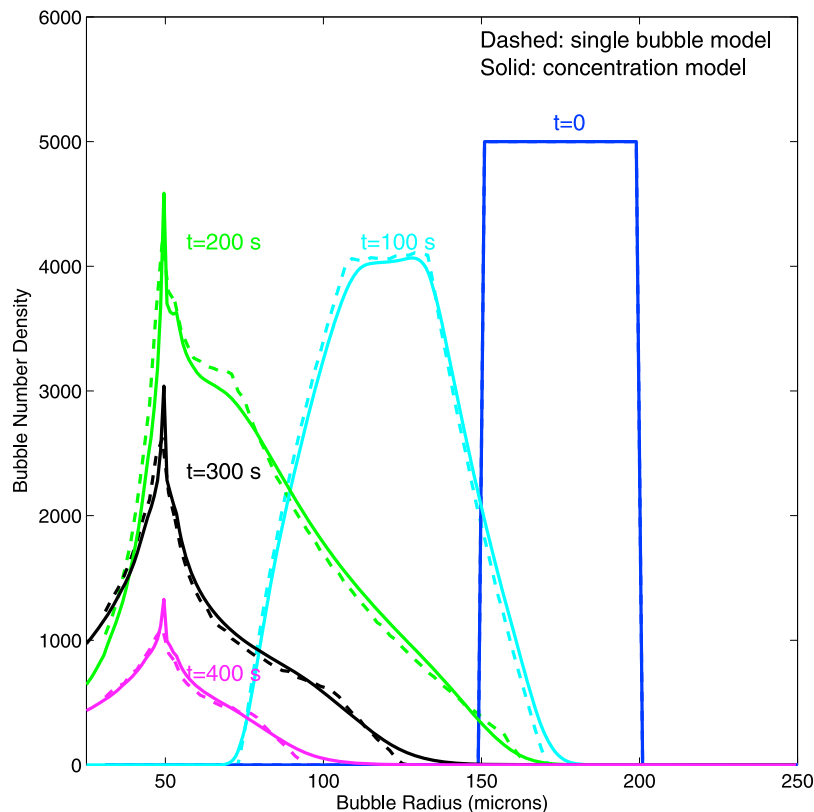


Figure 2. The evolution of the bubble size spectrum in the case simulating a single bubble cloud under a downwelling current.

water (Figures 1c and 1d) as a result of hydrostatic pressure and surface tension exerted on bubbles. The ratio between N_2 and O_2 increases in the first 75 s (Figure 1d). O_2 has a larger solubility than N_2 while the diffusivity of the two gases are close in magnitude, so the amount of O_2 in bubbles decreases faster than that of N_2 in bubbles and the percentage of O_2 in bubbles (χ_1) decreases. The decrease in χ_1 and the increase in χ_2 lead to the decrease in O_2 partial pressure and the increase in N_2 partial pressure in bubbles. Subsequently, the O_2 dissolution rate (dn_1/dt) decreases relative to the N_2 dissolution rate (dn_2/dt), as can be seen in equation (4). After 75 s, N_2 dissolves faster, and the ratio between N_2 and O_2 gradually decreases to its atmospheric value.

[21] Figure 2 displays the evolution of the bubble number spectrum in the total water column. The results from the two models again agree well with each other. According to the ideal gas law, the size of a bubble is determined by the gas amount in the bubble and the pressure exerted on it. The evolution of the bubble number spectrum shows that bubbles get smaller after they are released. The gas dissolution effect is dominant over the decreasing ambient water pressure when bubbles rise. The distribution spreads in the size (radius) direction in the first 100 s because bubbles of the same size at different depths have different rates of size change (refer to equations (4) and (5)). After 200 s, there is a peak near 50 μm in the bubble size spectrum. Bubbles of about 50 μm are more abundant in the water. Bubbles smaller than 50 μm are brought down to greater depth and dissolve faster into the water than bubbles near 50 μm . Bubbles larger than 50 μm continue to rise and leave the water when they reach the surface.

[22] These test results show that our model is capable of accurately simulating bubble advection, gas dissolution from bubbles, buoyant rising and bubble size changes. The results also suggest that gases are able to dissolve into the 100% saturated water due to the large hydrostatic pressure and surface tension exerted on them. Although O_2 dissolves faster initially due to its larger solubility, N_2 dissolves faster when its fraction in bubbles gets larger.

4. Bubbles and Dissolved Gases After a Single Breaking Wave

[23] Bubbles injected by breaking waves play an important role in air-sea interaction. It has been observed and conjectured that bubbles injected by breaking waves greatly enhance dissolved gas concentration and air-sea gas transfer rate [e.g., Farmer *et al.*, 1993; Chiba and Baschek, 2010]. In this section, the evolution of bubbles and dissolved gases after an individual wave breaking event in an otherwise resting channel is modeled and studied.

4.1. Model Setup

[24] The configuration of the domain follows the laboratory experiments carried out in a hydraulic flume [Rapp and Melville, 1990; Lamarre and Melville, 1991; Deane and Stokes, 2002; Melville *et al.*, 2002; B. Baschek *et al.*, Direct laboratory seawater measurements of the dissolved CO_2 signature of individual breaking waves, submitted to *Journal of Geophysical Research*, 2010]. In those laboratory experiments, a wave-breaking event occurs due to the focusing of

Table 1. Boundary and Initial Conditions for Different Test Cases

| Test Case | Surface Gas Flux | Initial Saturation Level (%) |
|-----------|------------------|------------------------------|
| 1 | Yes | 100 |
| 2 | No | 100 |
| 3 | Yes | 99 |
| 4 | No | 99 |
| 5 | Yes | 101 |
| 6 | No | 101 |

a wave packet containing waves of different phase speeds [Rapp and Melville, 1990]. The position of the breaking event is controlled, and the breaking event is reproducible. The evolution of the velocity field [Melville et al., 2002] and bubble size distribution [Deane and Stokes, 2002] have been measured in those experiments.

[25] The dynamic flow model is the DNS model developed by Sullivan et al. [2004]. The DNS model solves the incompressible Navier-Stokes equations. The effect of a breaking wave on the velocity field is parameterized as a forward penetrating intrusion of momentum with the cross-breaking front shapes specified. It is fitted to the envelope observed in the laboratory experiments of Melville et al. [2002]. In the current run, the wavelength λ_0 , wave phase speed c_{waves} , and wave period τ_0 of the breaking wave are 2.3 m, 1.68 m/s and 1.37 s, respectively. These values are chosen to match the breaking waves generated in the experiment by Deane and Stokes [2002]. We use 100 grid points in both horizontal directions spanning 9.2 m ($4\lambda_0$); 96 surface intensified vertical levels covering the upper 4.6 m ($2\lambda_0$) with the smallest grid interval of 0.0115 m, and 40 stretched grids in the size direction covering 0 to 0.01 m with the smallest grid between 0 and 40 μm . Further refinement of the grids does not influence the results. The cutoff value of the simulated bubble size (0.01 m) matches the cutoff value of the observed bubble size distribution [Deane and Stokes, 2002]. Larger bubbles will quickly surface at the water surface after injection. From a perspective of air-sea gas exchange, bubbles are categorized by their fate [e.g., Sarmiento and Gruber, 2006; Emerson and Hedges, 2008]. Small bubbles that totally dissolve lead to “gas injection”, and large bubbles that eventually burst at air-water surface contribute to “gas exchange”. In the laboratory flow, bubbles of radius larger than 0.01 m are those responsible for exchange. In undersaturated to 100% saturated water, those bubbles help gas dissolution. In supersaturated water, those bubbles assist gas venting. We include three gases, N_2 , O_2 , and CO_2 in our calculation. The percentages of O_2 (χ_1^{atm}), N_2 (χ_2^{atm}) and CO_2 (χ_3^{atm}) in the atmosphere are [78.47%, 21.49%, 0.0385%]. Three runs at different initial gas saturation levels ($\sigma_m(t=0)$) (Table 1) have been carried out. The piston velocity for CO_2 , k_3 , is chosen to be 8.33×10^{-6} m/s (3 cm/h). This value is obtained from the formula suggested by Wanninkhof et al. [2009] assuming no sea surface wind. Piston velocity k_m of other gases can be calculated as $k_m = \sqrt{\frac{Sc_m}{Sc_3}} k_3$, where Sc is the Schmidt number [Wanninkhof et al., 2009]. To separate the contribution of bubbles to the gas flux, three more runs without surface diffusive flux ($k_m = 0$) are carried out.

[26] The parameterization for the bubble injection rate follows similar conventions as the momentum injection devised by Sullivan et al. [2004] and is

$$Q = Q_0 T(t) \mathcal{X}(x) \mathcal{Y}(y) \mathcal{L}(z) \mathcal{R}(r), \quad (11)$$

where Q_0 is the total bubble volume injection rate; T , \mathcal{X} , \mathcal{Y} , \mathcal{L} , and \mathcal{R} are the distribution functions in time (t), space (x, y, z), and radius (r), respectively, with x the direction of a breaking wave. Q_0 is chosen to match the observed void ratio of 0.1 in the upper 0.1 m right after breaking [Deane and Stokes, 2002]. The injection spans the x direction for one wavelength, 0.1 wavelength in depth, and one wave period in time. The temporal and spatial distribution functions are the same as those of the momentum injection [Sullivan et al., 2004, equation (3.3)]. The bubble size distribution function matches the observed bubble size spectrum right after wave breaking [Deane and Stokes, 2002]

$$\mathcal{R}(r) \propto \begin{cases} r^{-3/2} & \text{when } r \geq r_H \\ r^{-10/3} & \text{when } r < r_H, \end{cases} \quad (12)$$

where $r_H = 1$ mm is the observed Hinze scale [Deane and Stokes, 2002]. These two distinct scaling laws come from two different physical processes for bubble formation. Bubbles larger than the Hinze scale are formed by the fragmentation of large cavities under a breaker, while bubbles smaller than the Hinze scale are entrained into the water by the plunging jet of a breaking wave [Deane and Stokes, 2002].

4.2. The Evolution of Bubbles

[27] The bubble size spectrum immediately after bubble injection and 1.5 s later are shown in Figure 3a. The water is open to the air in the lab experiment [Deane and Stokes, 2002], so it is assumed that the water is 100% saturated. The measured distributions [Deane and Stokes, 2002] are also plotted in Figure 3a. It can be seen that the computed solutions compare well with the laboratory measurements. After bubbles are injected, large bubbles rise and leave the water more rapidly than small bubbles. This preferential loss of large bubbles results in the rapid steepening of the bubble size distribution shown in Figure 3a. All bubbles larger than 2 mm leave the water after 1.5 s (about $1.1\tau_0$). Bubbles larger than 0.3 mm leave the water after 10 s (about $7.3\tau_0$). Figure 3b displays the evolution of the associated total bubble volume. The total bubble volume decreases significantly immediately after bubble injection due to the rapid loss of large bubbles. After 1.5 s (about $1.1\tau_0$), the total void volume is below 1% of the total void volume just after bubble injection. Although most air leaves the water with large bubbles in the first few seconds, there are still abundant small bubbles in the water, as can be seen in Figure 3a.

[28] Figure 4 (top) shows the velocity fields in the $x-z$ plane at $t = 11\tau_0$. The momentum impulse exerted by the breaking wave has been experimentally and numerically investigated by Melville et al. [2002] and Sullivan et al. [2004], respectively. A breaking wave generates a vortex in the cross-wave direction in the water. This vortex propagates downstream at a speed of approximately 8×10^{-3} of the wave phase speed. Our current results are in good agreement with

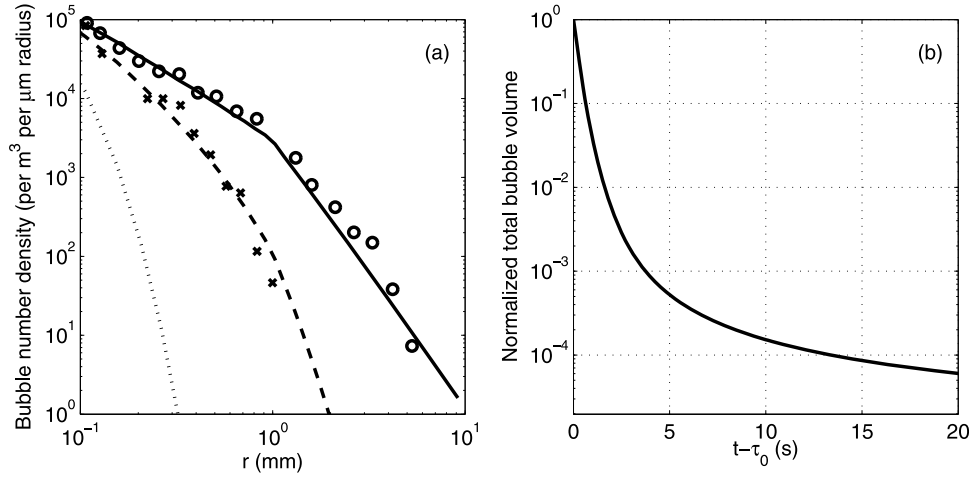


Figure 3. The evolution of (a) the bubble size spectrum (solid line is the computed solutions right after wave breaking, dashed line is the computed solutions 1.5 s after wave breaking, dotted line is the computed solutions 10 s after wave breaking, circles are the data right after breaking from the measurements of *Deane and Stokes* [2002], and crosses are the data 1.5 s after breaking from the measurements of *Deane and Stokes* [2002]). (b) Total bubble volume normalized by the bubble volume immediately after the wave breaking in the single-breaker simulation.

the two previous studies. Figure 4 (bottom) shows the number density of 63 μm bubbles at the same time. It can be seen that there are still large amount of bubbles of this size close to the breaker-generated vortex. There are much more bubbles at the downward branch of the breaker-generated vortex than at the upward branch of the vortex. After bubbles are subducted by the vortex, they dissolve more quickly than when they are at the surface.

4.3. The Evolution of Dissolved Gases in Saturated Water

[29] Figures 5a–5c show the evolution of the absolute and relative anomaly of dissolved gases and dissolved inorganic

carbon (DIC) in runs 1 and 2 where the water is 100% saturated. The absolute anomaly of dissolved O₂, dissolved N₂, and DIC are calculated as $\Delta c_m^{tot}(t) = \int c_m(t, \vec{x}) dV - \int c_m(0, \vec{x}) dV$ and is shown on the left vertical axis of Figures 5a–5c. The relative anomaly is calculated as $\frac{\Delta c_m^{tot}(t)}{c_m^{inj}}$, where c_m^{inj} is the total amount of gas in injected bubbles. This quantity is shown on the right vertical axis of Figures 5a–5c. Δc_m^{tot} can also be interpreted as the total amount of gas dissolution. Figure 5d shows the absolute dissolved CO₂ anomalies calculated as $\Delta c_3^*(t) = \int c_3^*(t, \vec{x}) dV - \int c_3^*(0, \vec{x}) dV$, and similarly, the relative dissolved CO₂ anomalies calculated as $\frac{\Delta c_3^*(t)}{c_m^{inj}}$. There is no noticeable difference between the results from run 1 and

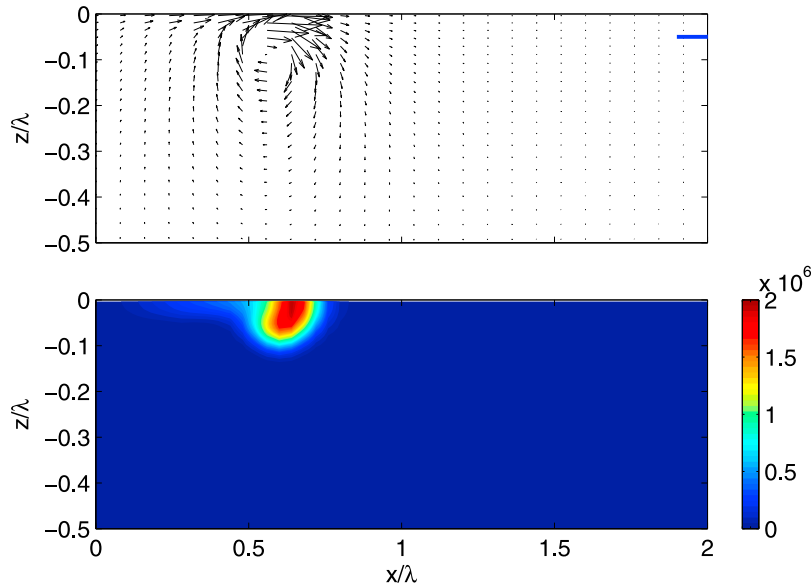


Figure 4. (top) Velocity field and (bottom) the number density of 63 μm bubbles (number of bubbles per unit volume per 1 μm radius increment) at t = 11τ₀. The blue bar in the upper right corner of Figure 4 (top) indicates 0.04 × c_{wave}.

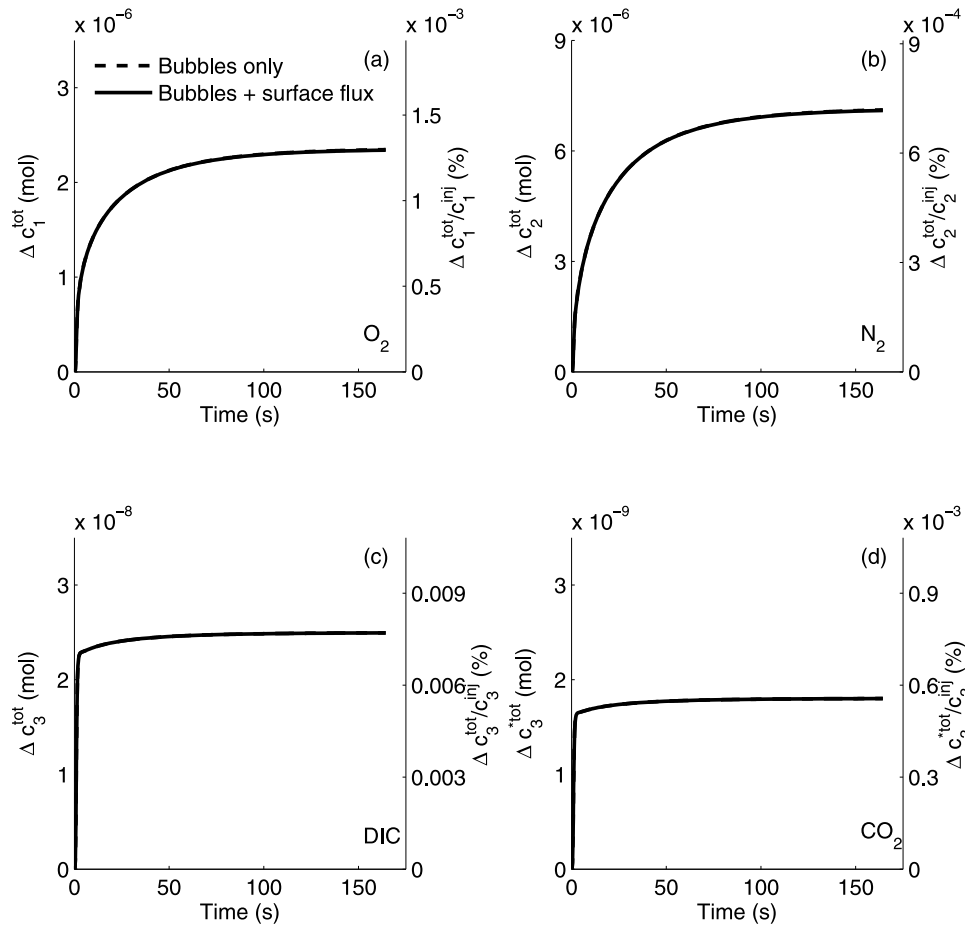


Figure 5. The time evolution of the absolute and relative anomaly of (a) dissolved O_2 , (b) dissolved N_2 , (c) DIC, and (d) dissolved CO_2 for runs 1 (solid line) and 2 (dashed line) where the water is 100% saturated (the dashed lines are not seen because the solid and the dashed lines almost overlap).

run 2 because the water is 100% saturated. In contrast to the quick loss of most injected air in the first few seconds, the increases in dissolved gas amount due to bubbles gradually continue for more than 100 s for all three gases. Gases inside the remaining small bubbles continue to dissolve into the water after the large bubbles leave the water. Although the water is 100% saturated, gases inside the bubbles are able to dissolve into the water because the gases inside bubbles are compressed by both hydrostatic pressure and surface tension in addition to the atmospheric pressure. Δc_m^{tot} is largest for N_2 and smallest for CO_2 because N_2 is the most common gas in the atmosphere and CO_2 is the least common gas among the three gases. However, $\frac{\Delta c_m^{tot}}{c_m^{inj}}$ is smallest for N_2 and largest for CO_2 because N_2 is the least soluble and CO_2 is the most soluble among the three gases. More than 90% of the total CO_2 dissolution takes place in the first 10 s. The dissolved CO_2 anomaly is a little bit more than 1 order of magnitude smaller than the total amount of CO_2 dissolution. Large portion of dissolving atmospheric CO_2 stays in the form of HCO_3^- and CO_3^{2-} and less than 10% stays as dissolved CO_2 .

[30] Figures 6–8 show the velocity fields and the saturation anomaly (σ'_m) of the three gases at $t = 2\tau_0$, $t = 11\tau_0$, and $t = 51\tau_0$, respectively. The saturation anomaly is defined as $\sigma'_m(t) = \sigma_m(t) - \sigma_m(0)$. Figures 6a, 7a, and 8a show velocity fields in the $x-z$ plane and Figures 6b–6d, 7b–7d,

and 8b–8d show the evolution of σ'_m . The maximum σ'_m is largest for N_2 and smallest for CO_2 , because the solubility is smallest for N_2 and largest for CO_2 . The maximum σ' for CO_2 is almost 2 orders of magnitude smaller than for O_2 and N_2 as a considerable amount of CO_2 after dissolution is in the form of CO_3^{2-} and HCO_3^- . The dissolved gas anomalies are advected in the wave direction by the breaker induced vortex. The maximum enhancement of the dissolved gases stays near the subsurface core of the vortex. At $t = 11\tau_0$, the location of maximum σ' is between the downward branch and the core of the breaker-generated vortex. This signal is a combined effect of advection of dissolved gas anomaly by the breaker-generated vortex and the local dissolution from bubbles brought down by the downward current. At $t = 51\tau_0$, the location of maximum σ' is at the center of the breaker-generated vortex. While propagating downstream, the maximum σ' decreases and the area of positive σ' increases (compare Figures 6 and 7). The dissolved gas anomalies diffuse into the surrounding water.

4.4. The Evolution of Dissolved Gases in Undersaturated Water

[31] Figure 9 shows the evolution of Δc_m^{tot} and $\frac{\Delta c_m^{tot}}{c_m^{inj}}$ in runs 3 and 4 where the water is 1% undersaturated. The amount of gas dissolution through bubbles when the water is at this

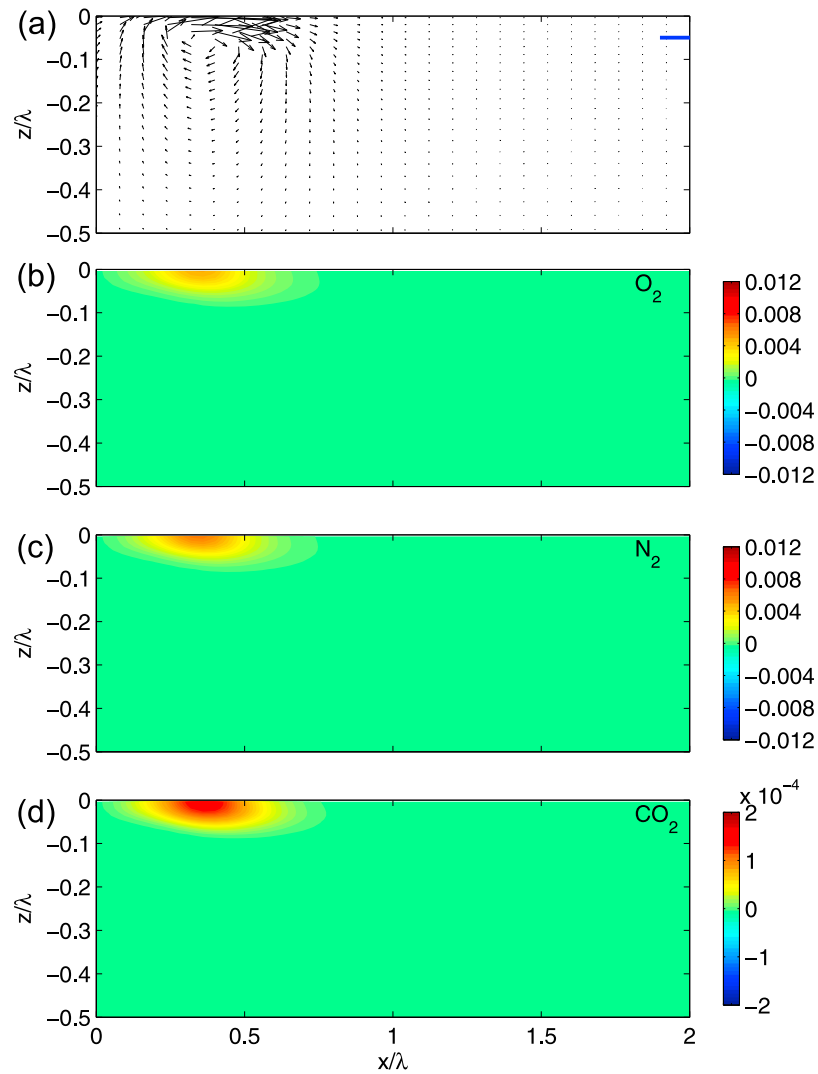


Figure 6. (a) Velocity field and saturation anomalies (σ' defined in the text) for (b) O_2 , (c) N_2 , and (d) CO_2 at $t = 2\tau_0$ from test 1 where the water is 100% saturated. The blue bar in the upper right corner of Figure 6a indicates $0.04 \times c_{wave}$.

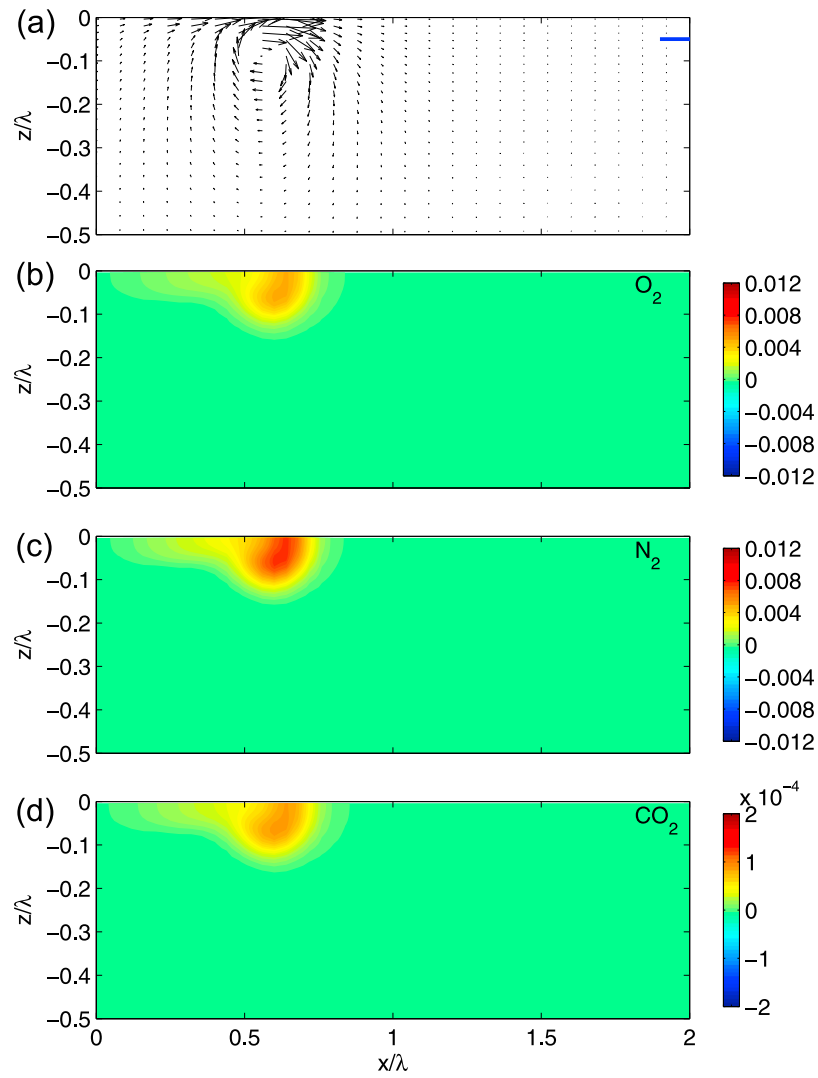


Figure 7. The same as Figure 6 except for $t = 11\tau_0$.

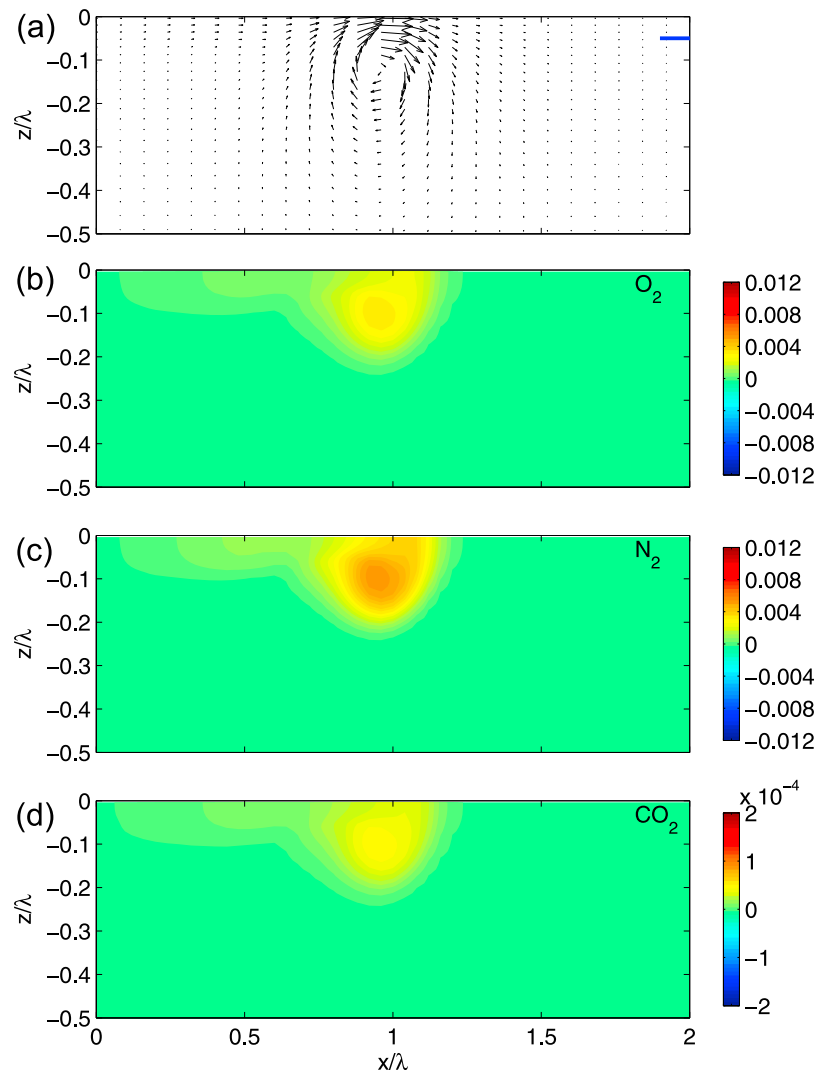


Figure 8. The same as Figure 6 except for $t = 51\tau_0$.

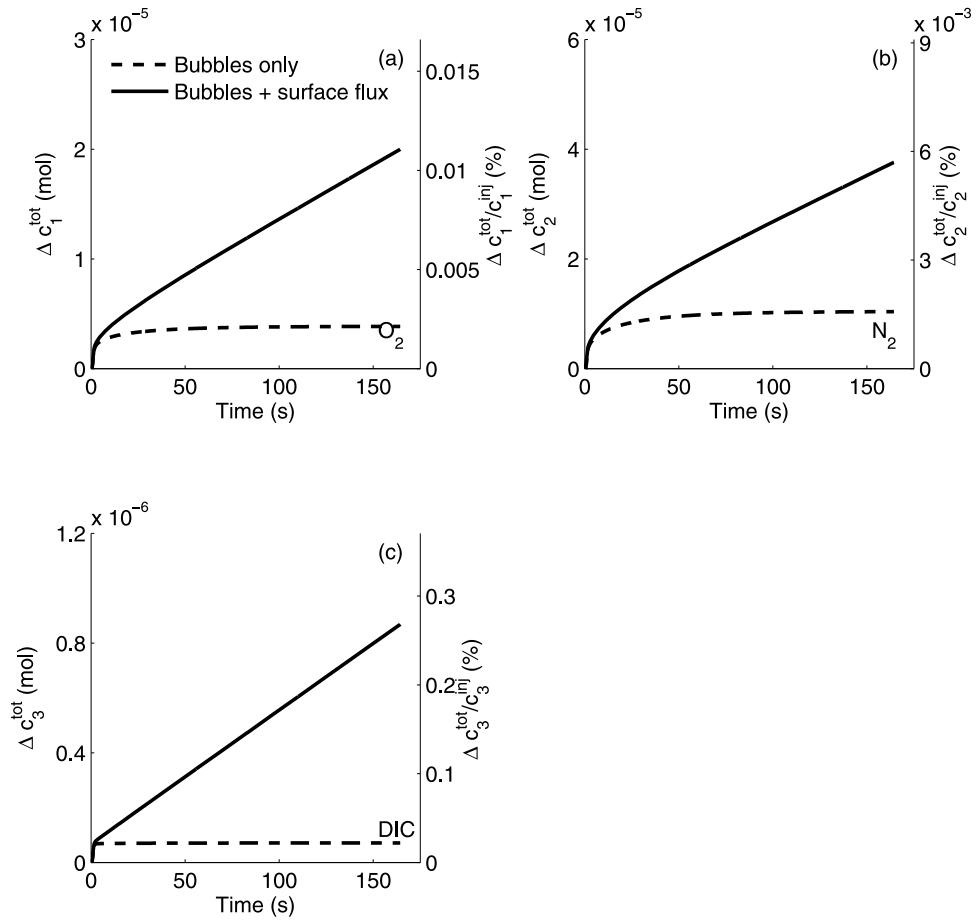


Figure 9. The time evolution of the absolute and relative anomaly of (a) dissolved O_2 , (b) dissolved N_2 , and (c) DIC from runs 3 (solid line) and 4 (dashed line) where the water is 1% undersaturated.

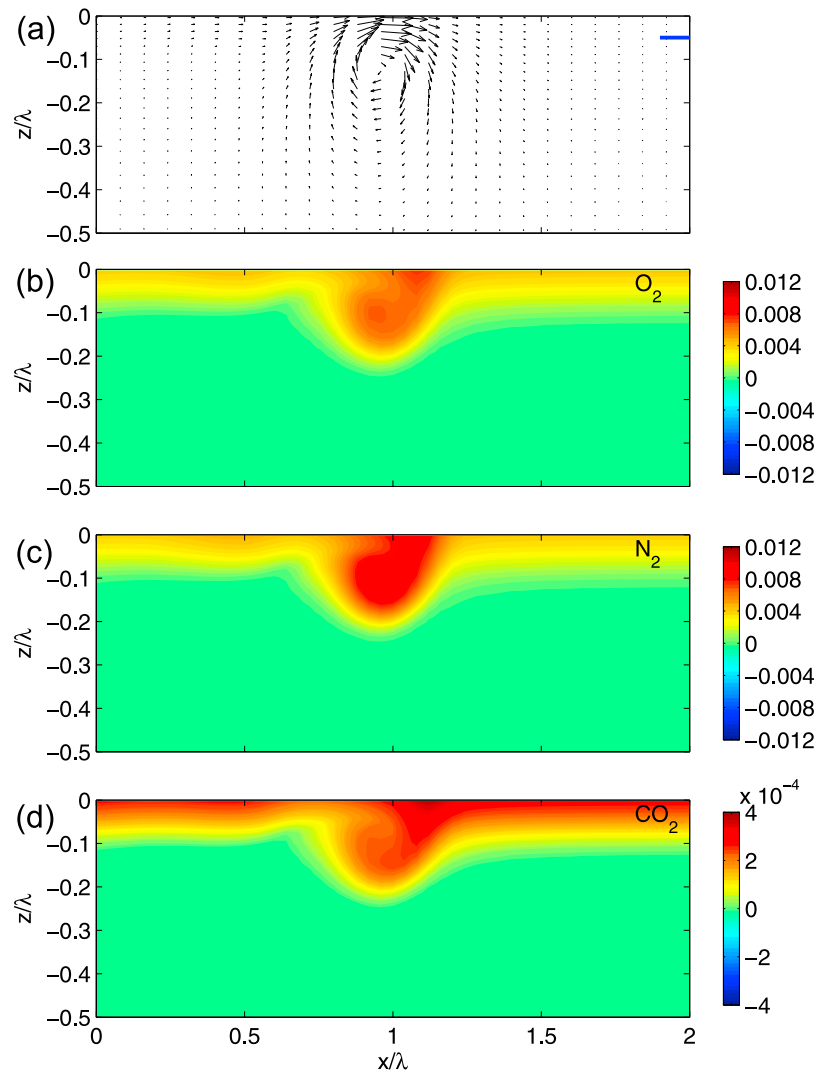


Figure 10. (a) Velocity field and saturation anomalies (σ' defined in the text) for (b) O_2 , (c) N_2 , and (d) CO_2 at $t = 51\tau_0$ from test 3 where the water is 1% undersaturated. The blue bar in the upper right corner of Figure 10a indicates $0.04 \times c_{wave}$.

saturation level is larger than when the water is 100% saturated. It is 2.7 times larger for O_2 , 2.3 times for N_2 , and 5.4 times for CO_2 . The bubble–water gas concentration difference is larger in undersaturated water than in 100% saturated water, thus the dissolution rate through bubbles is larger in undersaturated water. The bubble contribution to the total gas flux at $t = 50$ s ($36.5\tau_0$) is approximately 43% for O_2 , 54% for N_2 , and 23% for CO_2 . The solubility of N_2 is smallest, and the diffusive gas transfer at the surface is smallest relative to the amount of total injected gas. The bubble contribution drops to 21%, 29%, and 9% after 150 s ($109.5\tau_0$). Between 50 s and 150 s, the contribution of bubbles to the total gas flux is tiny while gases continue to dissolve into water at the water surface. It implies that the bubble contribution to air–sea gas flux is larger when wave breaking occurs more frequently given the same surface diffusive gas flux.

[32] Figure 10 shows the velocity fields and σ'_m at $t = 51\tau_0$. There is a layer of positive dissolved gas anomaly near the surface due to the surface diffusive gas transfer. The breaker generated vortex not only advects the positive dissolved gas

anomalies downstream, but also entrains the surface diffusive layer to a greater depth.

4.5. The Evolution of Dissolved Gases in Supersaturated Water

[33] Figures 11a, 11c, and 11e show the evolution of the absolute and relative total gas dissolution amounts in runs 5 and 6 where the water is 1% supersaturated. The total amount of gas dissolution is negative for all three gases in run 5 as the partial pressure of the dissolved gases are larger than the atmospheric partial gas pressures. Dissolved gases diffuse out of the water through the surface. The integrated bubble contribution is positive for both O_2 and N_2 , but is negative for CO_2 . Figures 11b, 11d, and 11f are close-ups of Figures 11a, 11c, and 11e for the first 20 s. It can be seen that the total bubble-mediated gas flux is negative for the first 8 s for O_2 , and 5 s for N_2 . Dissolved gases between the surface and 0.1 m are possible to diffuse into the bubbles larger than $140 \mu\text{m}$ that are abundant in the first few seconds. Either the hydrostatic pressure at depth greater than 0.1 m or the surface

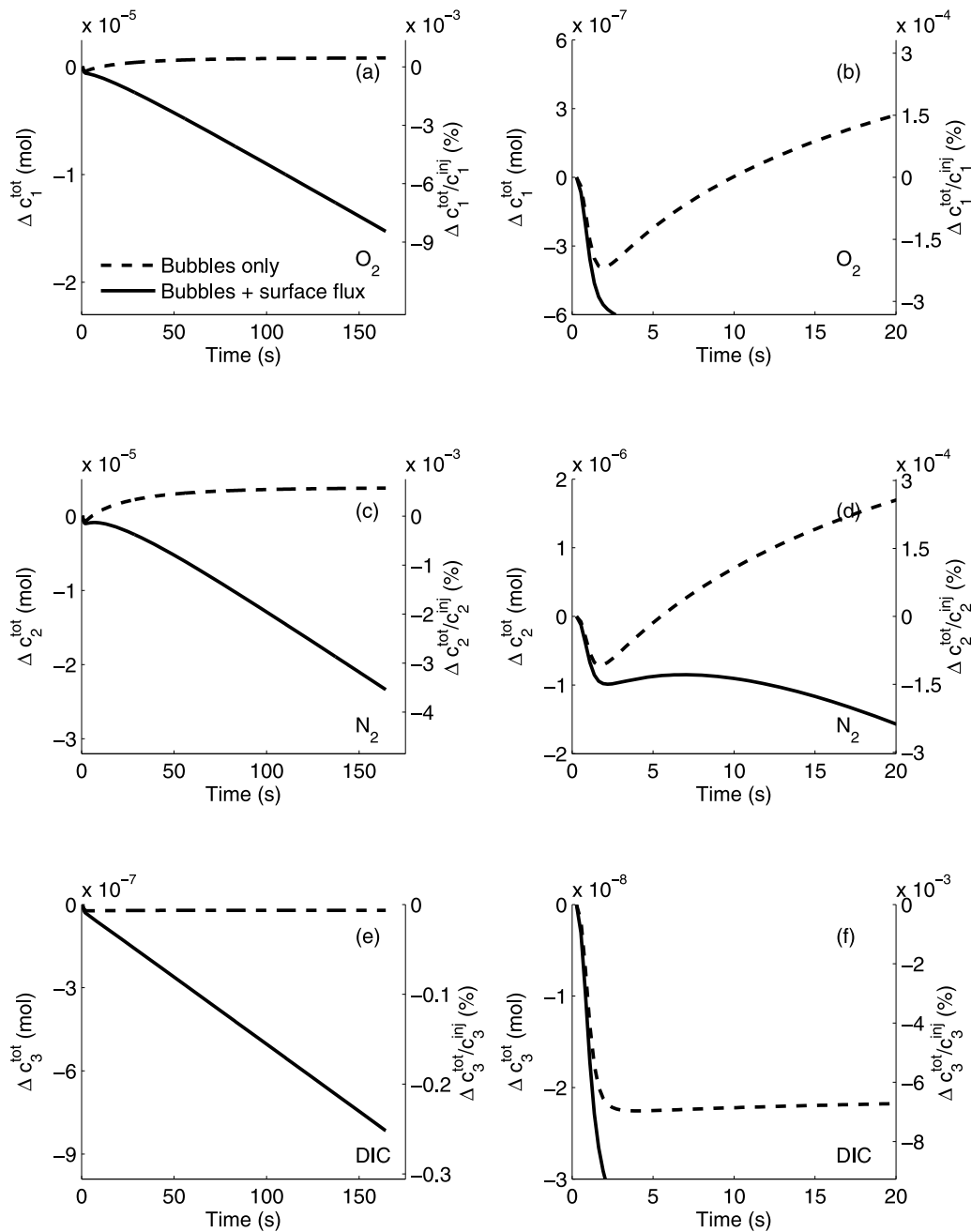


Figure 11. The time evolution of the absolute and relative anomaly of (a) dissolved O_2 , (c) dissolved N_2 , and (e) DIC for runs 5 (solid line) and 6 (dashed line) where the water is 1% supersaturated. Close-ups of Figures (b) 11a, (d) 11c, and (f) 11e are also shown.

tension of bubbles smaller than $140 \mu\text{m}$ is sufficient to counteract the 1% supersaturated dissolved gas pressure. The venting of dissolved gas through bubbles dominates the dissolution from bubbles in the first 3 s when Δc_m^{tot} decreases for all three gases in run 6 (Figures 11b, 11d, and 11f). The relative amount of CO_2 bubbles vented out is much larger than the relative amounts of O_2 or N_2 bubbles vented out, because the solubility of CO_2 is much larger. After the large bubbles leave the water, the dissolution effect due to small bubbles dominates and the total bubble contribution gradually increases. The integrated effect of bubbles is dissolution for

the less soluble O_2 and N_2 , and venting for the more soluble CO_2 .

[34] Figure 12 shows the velocity fields and σ'_m of the dissolved gases at $t = 51\tau_0$. The breaker generated vortex entrains the negative dissolved gas anomaly to greater depth. At the subsurface core of the breaker generated vortex, the negative dissolved gas anomalies are smaller than the surrounding water. In fact, the dissolved gas anomalies are positive for O_2 and N_2 at the subsurface core of the breaker-generated vortex. This is due to the dissolution of gases from small bubbles.

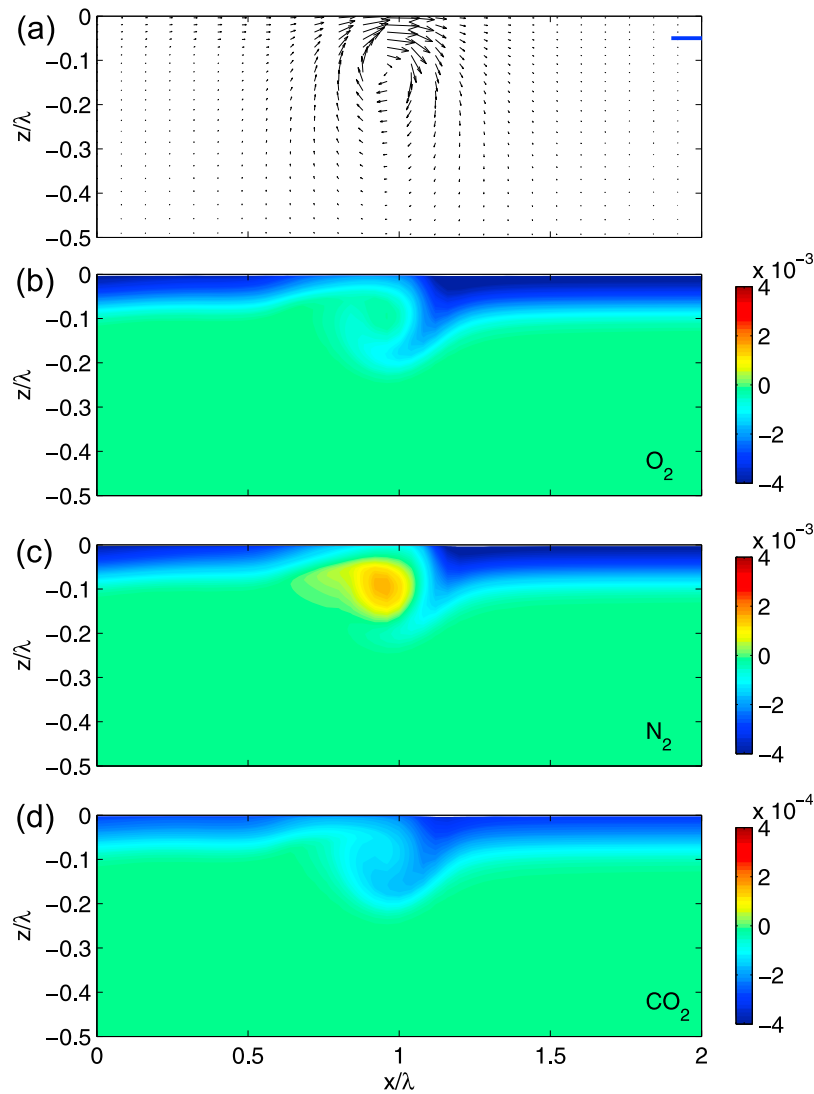


Figure 12. (a) Velocity field and saturation anomalies (σ' defined in the text) for (b) O_2 , (c) N_2 , and (d) CO_2 at $t = 51\tau_0$ from test 5 where the water is 1% supersaturated. The blue bar in the upper right corner of Figure 12a indicates $0.04 \times c_{wave}$.

4.6. Implication for Air-Sea Gas Exchange

[35] The model results shown in this section imply that bubbles are important for air-sea gas exchange by enhancing both the equilibrium saturation level and the gas transfer rate.

[36] We here define σ_m^b as the saturation level at which the total bubble contribution to the total gas flux is zero. σ_m^b depends on the solubility of the gas as well as bubble penetration depth. It is smaller for more soluble gases like CO_2 and for shallower bubble penetration. σ_m^b is larger than the equilibrium saturation level σ_m^{eq} [Keeling, 1993; Woolf, 1997] at which the net gas flux, including the bubble contribution, is zero. In the presence of bubbles, both σ_m^b and σ_m^{eq} are slightly higher than 100%. When $\sigma_m < 100\%$, both the gas fluxes through bubbles and through water surface are from the atmosphere to the water, and bubbles provide an additional pathway for gas dissolution from the atmosphere. When $100\% \leq \sigma_m \leq \sigma_m^b$, the integrated bubble effect is interior gas dissolution with outgassing at the water surface. The net gas

transfer is ingassing when $\sigma_m < \sigma_m^{eq}$ and outgassing when $\sigma_m > \sigma_m^{eq}$. When $\sigma_m > \sigma_m^b$, bubbles add to the venting of dissolved gases. For the bubbly flows generated by an individual breaking wave in the laboratory channel, $\sigma_m^b > 101\%$ ($m = 1$ and 2), and $100\% < \sigma_3^b < 101\%$.

[37] In order to quantify the bubble contributions to the air-water gas flux in the channel, we calculate the bubble-induced gas flux under a breaking wave as $F_m^b = \frac{\Delta c_m^{tot}(t=\infty)}{\lambda^2 \tau_0}$ ($m = 1, 2$, and 3), where F_m^b is positive for gas flux from bubbles to water; Δc_m^{tot} is the domain integrated dissolved O_2 , N_2 , and DIC enhancement in the runs without surface flux (i.e., runs 2, 4, and 6). At $t = \infty$, bubbles have either fully dissolved or burst at the surface, thus Δc_m^{tot} represent the total changes in dissolved gases due to all injected bubbles. The gas flux at the air-water interface is calculated using the initial air-water gas concentration difference as $F_m^{sfc} = k^{sfc} (1 - \sigma_m(t=0)) c_m^*(t=0)$ ($m = 1, 2$, and 3) with k^{sfc} the gas transfer rate due to diffusion at the air-water interface. The two different fluxes for the three different gas saturation

Table 2. Gas Flux Through the Air-Water Interface F_m^{sfc} and Through bubbles F^b in Different Initial Gas Saturations

| Initial Saturation | Gas | F_m^{sfc} (mol/m ³ m/s) | F^b (mol/m ³ m/s) |
|--------------------|-----------------|--------------------------------------|--------------------------------|
| 100% | O ₂ | 0 | 4.98×10^{-7} |
| | N ₂ | 0 | 1.51×10^{-6} |
| | CO ₂ | 0 | 5.28×10^{-9} |
| 99% | O ₂ | 1.96×10^{-8} | 8.16×10^{-7} |
| | N ₂ | 3.75×10^{-8} | 2.20×10^{-6} |
| | CO ₂ | 1.08×10^{-9} | 1.51×10^{-8} |
| 101% | O ₂ | -1.96×10^{-8} | 1.77×10^{-7} |
| | N ₂ | -3.75×10^{-8} | 8.05×10^{-7} |
| | CO ₂ | -1.08×10^{-9} | -4.4×10^{-9} |

levels are shown in Table 2. The gas fluxes due to bubbles are much larger than the gas fluxes at the air-water interface for all three gases and all three initial saturation levels, partly because the air-water gas concentration differences are small and we consider only the area of wave breaking. When the water is 100% saturated, the interfacial gas fluxes are zero, while the bubble-induced gas fluxes are positive. When the water is undersaturated, the ratio between bubble flux and surface flux is largest for the least soluble N₂. Since σ_m^b is bigger than 101% for O₂ and N₂, bubble-induced gas fluxes are positive for these two gases when the water is 1% supersaturated. Bubble flux is negative for CO₂ at this saturation level since σ_3^b is smaller than 101%.

[38] Those values for σ_m^b , F_m^b , and F_m^{sfc} obtained for the laboratory channel flow are not representative of values for the real oceans. The whitecap coverage, i.e., the fraction of breaking waves, is at the order of 1% at a wind speed of 20 m/s and increase with wind speed [e.g., *Monahan, 2001*]. Most of the breaking waves in the ocean are larger than the one generated in the laboratory and inject bubbles to a greater depth. There are other dynamical processes than a breaker-generated vortex. Some of these processes, e.g., the downward branches of Langmuir cells, can subduct more and larger bubbles than a breaker-generated vortex can. F_m^b is larger when the whitecap coverage is larger and bubbles are subducted to greater depth. The surface transfer coefficient (k_m^{sfc}) is also significantly larger when there is wind. The effect of all these factors and an accurate estimate of σ_m^b as well as F_m^b would require a model configuration with more realistic surface forcing and boundary layer turbulence.

5. Summary

[39] We present a size-resolving bubble model and a dissolved gas model. The bubble model solves a set of equations for the concentrations of different gases in bubbles of different sizes. It includes the effects of advection, diffusion, bubble buoyant rising, bubble size change, and gas exchange between bubbles and dissolved gases. Bubble number concentration is calculated at each time step. The dissolved gas model includes the effects of advection, diffusion, surface diffusive flux, and gas exchange between bubbles and dissolved gases. These two models are coupled by the gas exchange between bubbles and dissolved gases. The concentration of dissolved CO₂ is diagnosed at each time step using reactions in inorganic carbon chemistry.

[40] The model consistency and numerical accuracy are tested by comparing the model results with solutions from an individual bubble model in a test simulating a bubble cloud

containing O₂ and N₂ with an idealized size distribution released at 5 m to 10 m depth. The two models agree well in all comparisons. It is shown that the more soluble O₂ dissolves faster at the beginning, but both N₂ and O₂ get close to their initial partitions in the long term.

[41] The bubble model and the dissolved gas model are coupled with a DNS flow model to simulate the flow, bubble, and dissolved gas evolution after a wave-breaking event. Bubbles with O₂, N₂, and CO₂ are injected during wave breaking. The initial bubble size spectrum is chosen to match experimental measurements. The computed bubble size spectrum 1.5 s after injection agrees well with the measured one. The void fraction decreases dramatically right after the breaking event and drops to less than 1% within 2 s after breaking. However, the enhancement in the dissolved gases continues for more than 100 s when the water is saturated. The breaker-generated vortex advects both bubbles and dissolved gas anomalies downstream. Bubbles are more concentrated at the downward branch than the upward branch of the vortex. Dissolved gas anomalies also diffuse into the ambient water with time. When the water is not 100% saturated, the vortex also entrains the surface diffusive layer to a greater depth. The modeling results show that bubbles are important for air-sea gas exchange and dissolved gas dynamics in the upper ocean. Due to the hydrostatic pressure and surface tension exerted on bubbles, gases inside bubbles are able to dissolve in slightly supersaturated water. When the water is highly supersaturated, bubbles add to the venting of dissolved gases.

[42] Bubbles in the real ocean evolve under the influence of more dynamical processes than wave breaking. They are able to weaken the downwelling branch of Langmuir cells when they are abundant [*Smith, 1998*]. They are also capable of enhancing the gas flux from the atmosphere to the ocean due to the hydrostatic pressure of the water column and the surface tension of the bubbles exerting on gases inside bubbles [*Wanninkhof et al., 2009*]. The bubble mediated gas transfer is especially important when the water is at near- to slightly supersaturation level. With a model capable of capturing the essential bubble physics and the simultaneous evolution of dissolved gas concentration, we will continue to explore the dynamic effects of bubbles in a turbulent ocean by coupling the model developed in this study with Large Eddy Simulation models [*Sullivan and McWilliams, 2010*], and also improve the understanding and parameterization of air-sea gas exchange in the bubble-mediated regime.

[43] **Acknowledgments.** This work is supported by the Office of Naval Research through contract N00014-08-1-0597. J.-H.L. also acknowledges the support by NCAR when he visited NCAR as an ASP graduate student visitor. Computation in this study was performed on NCAR's supercomputer Bluefire. NCAR is sponsored by the National Science Foundation.

References

- Baschek, B., D. M. Farmer, and C. Garrett (2006), Tidal fronts and their role in air-sea gas exchange, *J. Mar. Res.*, *64*, 483–515.
- Chiba, D., and B. Baschek (2010), Effect of Langmuir cells on bubble dissolution and air-sea gas exchange, *J. Geophys. Res.*, *115*, C10046, doi:10.1029/2010JC006203.
- Coleman, G. N., J. H. Ferziger, and P. R. Spalart (1990), A numerical study of the turbulent Ekman layer, *J. Fluid Mech.*, *213*, 313–348.

- D'Asaro, E., and C. McNeil (2007), Air-sea gas exchange at extreme wind speeds measured by autonomous oceanographic floats, *J. Mar. Res.*, *66*, 92–109.
- Deane, G. B., and M. D. Stokes (2002), Scale dependence of bubble creation mechanisms in breaking waves, *Nature*, *418*, 839–844.
- Emerson, S. R., and J. I. Hedges (2008), *Chemical Oceanography and the Marine Carbon Cycle*, Cambridge Univ. Press, Cambridge, U. K.
- Farmer, D. M., and M. Li (1995), Patterns of bubble clouds organized by Langmuir circulation, *J. Phys. Oceanogr.*, *25*, 1426–1440.
- Farmer, D. M., C. L. McNeil, and B. D. Johnson (1993), Evidence for the importance of bubbles in increasing air-sea gas flux, *Nature*, *361*, 620–623.
- Keeling, R. F. (1993), On the role of large bubbles in air-sea gas exchange and supersaturation in the ocean, *J. Mar. Res.*, *51*, 237–271.
- Lamarre, E., and W. K. Melville (1991), Air entrainment and dissipation in breaking waves, *Nature*, *351*, 469–472.
- Lamarre, E., and W. K. Melville (1994), Void-fraction measurements and sound-speed fields in bubble plumes generated by breaking waves, *J. Acoust. Soc. Am.*, *95*(3), 1317–1328.
- Li, M., C. Garrett, and E. Skvillingstad (2005), A regime diagram for classifying turbulent large eddies in the upper ocean, *Deep Sea Res.*, *52*, 259–278.
- McNeil, C., and E. D'Asaro (2007), Parameterization of air-sea gas fluxes at extreme wind speeds, *J. Mar. Syst.*, *66*, 110–121.
- McWilliams, J. C., P. P. Sullivan, and C.-H. Moeng (1997), Langmuir turbulence in the ocean, *J. Fluid Mech.*, *334*, 1–30.
- Melville, W. K., and P. Matusov (2002), Distribution of breaking waves at the ocean surface, *Nature*, *417*, 58–63.
- Melville, W. K., F. Veron, and C. J. White (2002), The velocity field under breaking waves: Coherent structures and turbulence, *J. Fluid Mech.*, *454*, 203–233.
- Memery, L., and L. Merlivat (1985), Modelling of gas flux through bubbles at the air-water interface, *Tellus Ser. B*, *37*, 272–285.
- Monahan, E. C. (2001), Whitecaps and foam, in *Encyclopedia of Ocean Sciences*, edited by J. Steele, S. Thorpe, and K. Turekian, pp. 3213–3219, Academic, San Diego, Calif.
- Rapp, R. J., and W. K. Melville (1990), Laboratory measurements of deep-water breaking waves, *Philos. Trans. R. Soc. London A*, *331*, 735–800.
- Sarmiento, J. L., and N. Gruber (2006), *Ocean Biogeochemical Dynamics*, Princeton Univ. Press, Princeton, N. J.
- Smith, J. A. (1998), Evolution of Langmuir circulation during a storm, *J. Geophys. Res.*, *103*, 12,649–12,668.
- Stanley, R. H. R., W. J. Jenkins, D. E. Lott III, and S. C. Doney (2009), Noble gas constraints on air-sea gas exchange and bubble fluxes, *J. Geophys. Res.*, *114*, C11020, doi:10.1029/2009JC005396.
- Sullivan, P. P., and J. C. McWilliams (2010), Dynamics of winds and currents coupled to surface waves, *Annu. Rev. Fluid Mech.*, *42*, 19–42.
- Sullivan, P. P., J. C. McWilliams, and C.-H. Moeng (1996), A grid-nesting method for large-eddy simulation of planetary boundary layer flows, *Boundary Layer Meteorol.*, *80*, 167–202.
- Sullivan, P. P., J. C. McWilliams, and W. K. Melville (2004), The oceanic boundary layer driven by wave breaking with stochastic variability. Part 1. Direct numerical simulations, *J. Fluid Mech.*, *507*, 143–174.
- Sullivan, P. P., J. C. McWilliams, and W. K. Melville (2007), Surface gravity wave effects in the oceanic boundary layer: Large-eddy simulation with vortex force and stochastic breakers, *J. Fluid Mech.*, *593*, 405–452.
- Terrill, E. J., W. K. Melville, and D. Stramski (2001), Bubble entrainment by breaking waves and their influence on optical scattering in the upper ocean, *J. Geophys. Res.*, *106*, 16,815–16,823.
- Thorpe, S. A. (1982), On the clouds of bubbles formed by breaking wind-waves in deep water, and their role in air-sea gas transfer, *Philos. Trans. R. Soc. London A*, *304*, 155–210.
- Thorpe, S. A., T. R. Osborn, D. M. Farmer, and S. Vagle (2003), Bubble clouds and Langmuir circulation: Observations and models, *J. Phys. Oceanogr.*, *33*, 2013–2031.
- Vagle, S., D. M. Farmer, and G. B. Deane (2001), Bubble transport in rip currents, *J. Geophys. Res.*, *106*, 11,677–11,689.
- Wanninkhof, R., W. E. Asher, D. T. Ho, C. Sweeney, and W. R. McGillis (2009), Advances in quantifying air-sea gas exchange and environmental forcing, *Annu. Rev. Mar. Sci.*, *1*, 213–244.
- Wolf, D. K. (1997), Bubbles and their role in gas exchange, in *The Sea Surface and Global Change*, edited by P. S. Liss and R. A. Duce, pp. 173–205, Cambridge Univ. Press, New York.
- Wolf, D. K., and S. A. Thorpe (1991), Bubbles and the air-sea exchange of gases in near-saturation conditions, *J. Mar. Res.*, *49*, 435–466.
- Wolf, D. K., I. S. Leifer, P. D. Nightingale, T. S. Rhee, P. Bowyer, G. Caulliez, G. de Leeuw, S. E. Larsen, M. Liddicoat, J. Baker, and M. O. Andreae (2007), Modelling of bubble-mediated gas transfer: Fundamental principles and a laboratory test, *J. Mar. Syst.*, *66*, 71–91.
- Zedel, L., and D. Farmer (1991), Organized structures in subsurface bubble clouds: Langmuir circulation in the open ocean, *J. Geophys. Res.*, *96*, 8889–8900.
- Zhang, X., M. Lewis, and B. Johnson (1998), Influence of bubbles on scattering of light in the ocean, *Appl. Opt.*, *37*, 6525–6536.

B. Baschek, J.-H. Liang, and J. C. McWilliams, Department of Atmospheric and Oceanic Sciences, University of California, Los Angeles, Mathematical Sciences Building, Room 7217, Los Angeles, CA 90095-1565, USA. (liangjh@atmos.ucla.edu)

P. P. Sullivan, Mesoscale and Microscale Meteorology Division, National Center for Atmospheric Research, PO Box 3000, Boulder, CO 80307-3000, USA.